Temperature Estimation of IPMSM by Using Fundamental Reactive Energy Considering Variation of Inductances

Hyun-Sam Jung, *Member, IEEE*, Hwigon Kim, *Student Member, IEEE*, Seung-Ki Sul, *Fellow, IEEE*, and Daniel J. Berry

***Abstract*—In this article, a method to estimate the temperature of an NdFeB magnet in an interior permanent magnet synchronous motor (IPMSM) has been developed in medium and high speed operating conditions. Fundamental reactive energy is newly brought out and directly used in the developed method to estimate the magnet temperature accurately, which results in higher sensitivity with respect to the magnet temperature variation compared to the conventional methods. It is because the variation of the reactive energy caused by the magnet temperature includes variations of inductances in addition to that of the magnet flux linkage. In the proposed method, a stator resistance error effect caused by a stator temperature is inherently removed without any additional temperature sensor on stator winding. Moreover, the proposed method is robust to an inverter nonlinearity effect and ac resistance effect. As a result, the proposed method can estimate the magnet temperature accurately in real time, even in load variation, regardless of the stator temperature variation. The magnet temperature estimation error has been less than 3.7 °C in the online estimation for 10 000 s under wide speed and torque variations.**

***Index Terms*—Electric vehicles, motor drives, temperature.**

I. Introduction

INTERIOR permanent magnet synchronous machines (IPMSMs) have been widely used as a traction motor in automotive industries for the last 20 years, because of higher torque density thanks to not only permanent magnet flux linkage but also the difference of *d*-axis and *q*-axis reluctances and wide operating speed range due to flux weakening capability at a higher speed.

NdFeB magnets are usually employed in IPMSMs for traction because of higher residual flux density and stronger intrinsic coercivity. However, the magnet is vulnerable to its temperature variation. The variations in residual flux density and intrinsic coercivity of magnet can be represented as (1), where temperature constants, α_{mag} and β_{mag}, are negative [1], [2]. It means that both the residual flux density, B_r, and the intrinsic coercivity, H_{ci}, decrease as the magnet temperature, T_{mag}, increases. In (1), a subscript, "20", means values at 20 °C.

$$\begin{aligned} B_r &= B_{r\_20}\left(1+\alpha_{\mathrm{mag}}\left(T_{\mathrm{mag}}-20^o\mathrm{C}\right)\right) \\ H_{ci} &= H_{ci\_20}\left(1+\beta_{\mathrm{mag}}\left(T_{\mathrm{mag}}-20^o\mathrm{C}\right)\right). \end{aligned} \tag{1}$$

The variations, according to the magnet temperature in (1), influence the characteristics of IPMSMs [3]–[8]. Torque from the permanent magnet of IPMSM, proportional to the magnetic flux of a magnet, would vary with the magnet temperature. The residual flux density, B_r, changes with the ratio, α_{mag}, of around $-0.1\%/^{\circ}\mathrm{C}$ in the case of NdFeB magnet. Therefore, the magnet temperature is essential to keep the accuracy of the torque control [4]–[8]. Besides, in order to prevent an irreversible demagnetization of the permanent magnet, which permanently reduces the residual flux density, the temperature of the magnet should be monitored. Therefore, monitoring the magnet temperature is important in dealing with not only the accuracy of torque control but also the reliability of a power train of a vehicle. There has been a lot of research about the magnet temperature estimation. Those are mainly classified into a thermal model method, [9]–[14], where lumped parameter thermal networks with simplified thermal models, a signal injection method, [15]–[22], and an observation method of permanent magnet flux linkage, [23]–[27]. These days, a machine learning algorithm is getting attention. These algorithms have been used to estimate temperatures, such as linear regression in [28], convolutional and recurrent neural networks in [29], long short-term memories in [30], and a difference-estimating feed-forward neural network in [31]. It is also one of the possible attempts to estimate the magnet temperature without explicit knowledge about mechanical systems.

Thermal models in [9]–[14] require knowledge regarding mechanical systems such as cooling systems, geometry, and materials. Therefore, thermal models are affected by environment and operating conditions [9], [10]. Because of these issues, the industries have interests in temperature estimation based on an electrical model such as a signal injection method and a method observing magnet flux linkage. Therefore, in this article, the

Manuscript received March 3, 2020; revised June 18, 2020 and August 22, 2020; accepted September 21, 2020. Date of publication October 1, 2020; date of current version January 22, 2021. Recommended for publication by Associate Editor S. C. Yang. *(Corresponding author: Hyun-Sam Jung.)*

Hyun-Sam Jung is with the Division of Electronics and Electrical Engineering, Dongguk University-Seoul, Seoul 04620, South Korea (e-mail: junghyunsam@dongguk.edu).

Hwigon Kim and Seung-Ki Sul are with the School of Electrical Engineering and Computer Science, Seoul National University, Seoul 08826, South Korea (e-mail: hwigon@eepel.snu.ac.kr; sulsk@plaza.snu.ac.kr).

Daniel J. Berry is with the General Motors Global Propulsion Systems, Pontiac, MI 48340 USA (e-mail: daniel.j.berry@gm.com).

Color versions of one or more of the figures in this article are available online at https://ieeexplore.ieee.org.

Digital Object Identifier 10.1109/TPEL.2020.3028084

temperature estimation method has been developed based on an electrical model of a machine.

In the magnet temperature estimation method based on an electrical model, a signal injection method is used at a low speed. In [15], a pulse voltage was intermittently injected, when the *d*-axis of a rotor was aligned at a-phase of a motor under no-load condition. In [16] and [17], influences caused by load current and speed were compensated. In this pulse injection method, the *d*-axis current was biased at a certain level to improve the sensitivity of the method, and oversampling is employed to measure current variation. In [18] and [19], the high-frequency resistance was utilized to estimate the magnet temperature by injecting high-frequency current or voltage. In [20], the magnetization state was estimated by using high-frequency resistance. In [21], the relation between high-frequency inductance and the magnet temperature was found and utilized in the magnet temperature estimation, and in [22], the temperature estimator based on the relation was implemented and demonstrated by online estimation. However, these methods are for low speed. In medium-speed and high-speed regions, the signal injection is not necessary because the rotating speed is high enough to calculate the flux linkages from the voltages.

The methods in [23]–[27] can be applied to medium-speed and high-speed regions. In these methods, the magnet flux linkage was utilized, which can be obtained by removing the stator winding resistance from the *q*-axis voltage equation in a steady state. In [23]–[26], the stator winding resistance variation, caused by the stator temperature, was compensated by measuring the stator winding temperature. Therefore, in this method, temperature sensors were required at stator windings. The methods assumed that a nonlinearity effect of an inverter was perfectly compensated and had no regard for an ac resistance effect reported in [32]. The other method in [27] removed the stator resistance effect by using the technique in [33]. In this method, the magnet flux linkage was calculated as assuming that the *d*-axis and *q*-axis inductances were constants regardless of the magnet temperature variation. Through these processes, the magnet flux linkage was obtained, and the magnet temperature was estimated by using the temperature coefficients, α_{mag}, in the previous researches, in [23]–[27].

In this article, it is shown and demonstrated that the inductances are also changed according to the magnet temperature, and it would result in a considerable error in the method without considering the inductance variation caused by the magnet temperature [27]. To utilize the inductance variation, fundamental reactive energy, itself, is newly brought out and exploited to estimate the magnet temperature [34] instead of directly using the magnet flux linkage used in the previous research [23]–[27]. Moreover, in the proposed method, the stator resistance effects are inherently removed without temperature sensors like [27] and [33]. Additionally, it has been proved that the proposed method is robust to the inverter nonlinearity effect. The rest of this article has been organized as follows. In Section II, a manufactured small scale motor with a magnet temperature measurement system has been briefly described, where the magnet temperature and stator temperature can be monitored even in rotating and load variations. In Section III, it is proposed that the temperature estimation method by using the fundamental reactive energy in considering variations of inductances. In Section IV, the proposed method has been implemented and verified in the small-scale motor. And the proposed method is validated and evaluated in an online estimation for 10 000 s.

TABLE I
PARAMETERS OF THE DESIGNED MOTOR

Parameter	Value
Pole	4
Rated torque	10 N·m
Rated speed at 310 V	1800 r/min
Magnet flux linkage (λ_{pm})	0.369 V·s
Stator resistance (R_s)	1.6 Ω

II. MAGNET TEMPERATURE MEASUREMENT SYSTEM

The small-scale test setup for the prototype motor has been developed to measure the temperature of the magnets in IPMSM [35]. A cross-section view of IPMSM under the study is shown in Fig. 1(a). For measuring the temperature of the magnets, 32 temperature sensors are directly attached at different locations of magnets. The positions of the magnet temperature sensors in a pole are illustrated as black circles of the rotor in Fig. 1(a). In this article, the average value of the measured magnet temperatures is used and denoted as $T_{\mathrm{mag\_}av}$, where a subscript, *av*, means an average value.

Furthermore, temperatures of the stator windings are also measured, which is denoted as green dots in Fig. 1(a). In this experimental setup, temperatures of all the windings in a pole are measured. The average value of the stator temperatures is denoted as T_{sw_av}. Type of the temperature sensor is a platinum temperature sensor (PTS), because of the small size and robustness against electro-magnetic interference (EMI). The error bound of the selected sensor itself is about ± 1.1 °C in the range from -50 to 150 °C. Fig. 1(b) shows the mainboard in the temperature measurement system. The board has been equipped with a low power digital signal processor (DSP) and 16 $\times$ A/D ports on the front side. On the backside, there are a Bluetooth module and two batteries. The motor parameters are listed in Table I. Detailed explanation about the structure and the performance of the sensing system is described in [35].

III. TEMPERATURE ESTIMATION BY USING FUNDAMENTAL REACTIVE ENERGY CONSIDERING INDUCTANCES

An IPMSM model in the rotor reference frame is modeled as (2), where λ_{pm} is the magnet flux linkage, L_{ds} and L_{qs} denote *d*-axis inductance and *q*-axis inductance, respectively, and ω_r is the rotating speed of a motor. The flux linkages would change due to variations of inductances, L_{ds} and L_{qs}, or magnet flux linkage, λ_{pm}, by the magnet temperature. It is a well-known fact that the magnet flux linkage among these components decreases with the temperature coefficients, α_{mag}, as the magnet temperature increases. It is because the magnet flux linkage is directly proportional to a residual flux density in magnets in a motor in (1). The other components are inductances L_{ds} and L_{qs}, which are functions of *d*-axis current and *q*-axis current, and include cross saturation effect as (2). In Section III-A, the

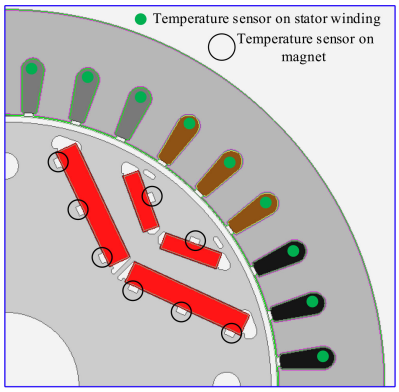

(a)

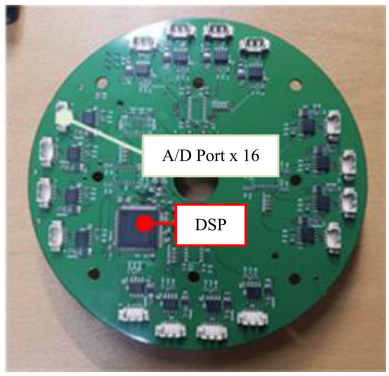

(b)

Fig. 1. Designed small-scale motor. (a) Its cross-sectional view in a pole and (b) the mainboard in the temperature measurement system.

inductances variations by the temperature have been described.

$$\begin{aligned} v_{ds}^r &= R_s i_{ds}^r + \frac{d}{dt}\lambda_{ds}^r - \omega_r \lambda_{qs}^r \\ v_{qs}^r &= R_s i_{qs}^r + \frac{d}{dt}\lambda_{qs}^r + \omega_r \lambda_{ds}^r \\ \text{where } \lambda_{ds}^r \left(i_{ds}^r,\, i_{qs}^r\right) &= L_{ds}\left(i_{ds}^r,\, i_{qs}^r\right) i_{ds}^r + \lambda_{pm} \\ \lambda_{qs}^r \left(i_{ds}^r,\, i_{qs}^r\right) &= L_{qs}\left(i_{ds}^r,\, i_{qs}^r\right) i_{qs}^r. \end{aligned} \tag{2}$$

A. Inductance Variation Caused by the Magnet Temperature

This section describes the inductance variation due to the magnet temperature. The stack length of the motor is assumed to be long enough for a simple explanation. This assumption makes sense for traction motors of electric vehicles (EVs). The inductances can be calculated by using a winding function and permeance. The permeance ideally has only even-order harmonics because an *N* pole and an *S* pole in a rotor have the same geometric structure. The winding function and the permeance of a-phase of a stator can be defined as (3), where ϕ_e is an angle from an arbitrary reference point along an air gap and θ_r is a rotor angle. The other phases can be represented by using a phase delay.

$$\begin{aligned} N_a\left(\phi_e\right) &= \sum_{h=1}^{\infty} N_h \cos\left(h\phi_e\right) \\ P\left(\phi_e,\, \theta_r\right) &= \left(P_0 + \sum_{k=1}^{\infty} P_{2k} \cos\left(2k\left(\phi_e - \theta_r\right)\right)\right) \\ L_{ds} &= L_{ls} + \frac{3}{2}\pi P_0 \left(N_1^2 + \sum_{k=1}^{\infty}\left({N_{3k+1}}^2 + {N_{3k-1}}^2\right)\right) \\ &\quad + \frac{3}{2}\frac{\pi}{2} P_2 {N_1}^2 \\ &\quad + \frac{3}{2}\frac{\pi}{2}\sum_{k=1}^{\infty}\left({N_{3k+1}}^2 P_{2(3k+1)}\right. \\ &\quad \left. + {N_{3k-1}}^2 P_{2(3k-1)}\right)\cos\left(6k\theta_r\right) \end{aligned} \tag{3}$$

$$\begin{aligned} L_{qs} &= L_{ls} + \frac{3}{2}\pi P_0 \left(N_1^2 + \sum_{k=1}^{\infty}\left({N_{3k+1}}^2 + {N_{3k-1}}^2\right)\right) \\ &\quad - \frac{3}{2}\frac{\pi}{2} P_2 {N_1}^2 \\ &\quad - \frac{3}{2}\frac{\pi}{2}\sum_{k=1}^{\infty}\left({N_{3k+1}}^2 P_{2(3k+1)}\right. \\ &\quad \left. + {N_{3k-1}}^2 P_{2(3k-1)}\right)\cos\left(6k\theta_r\right). \end{aligned} \tag{4}$$

From (3), the inductances have been derived in (4), and each inductance consists of dc components and multiples of sixth-order harmonics components, which is called as spatial harmonics. In the medium and high-speed regions, $6k\theta_r$ in (4) is substituted as $6k\omega_r t$. Therefore, the multiples of sixth-order harmonics in inductances can be easily filtered out by using a low pass filter. Therefore, only the dc components have been analyzed in this section, which can be calculated by harmonics in the winding function and dc component of permeance, P_0, and second-order harmonics in permeance, P_2, as derived in (4).

The permeance is the most sensitive variable with magnet temperature variation in (4) because the winding function variables, N_1, N_{3k-1}, and N_{3k+1}, are determined by winding configuration, which means that those variables are constants. The permeance can be represented by using a reluctance as (5). The reluctance variation caused by the magnet temperature variation can be written as (6), where k_c and k_m are geometrical parameters of flux paths.

$$P = \frac{1}{R} = \frac{1}{R_c + R_m + R_g} \tag{5}$$

$$\begin{aligned} \frac{dR}{dT_{\text{mag}}} &= -\frac{1}{\mu_0}\left(\frac{k_c}{{\mu_{rc}}^2}\frac{d\mu_{rc}}{dT_{\text{mag}}} + \frac{k_m}{{\mu_{\text{rec}}}^2}\frac{d\mu_{\text{rec}}}{dT_{\text{mag}}}\right) \\ &= -\frac{1}{\mu_0}\left(\frac{k_c}{{\mu_{rc}}^2} a_{\mu rc} + \frac{k_m}{{\mu_{\text{rec}}}^2} a_{\mu\text{rec}}\right) < 0. \end{aligned} \tag{6}$$

N40SH magnet has been used in the small-scale motor, and its B–H curve is shown in Fig. 2(a), where blue lines and red lines are intrinsic curves and normal curves regarding the magnet temperature, respectively. The recoil permeability, μ_{rec}, can be

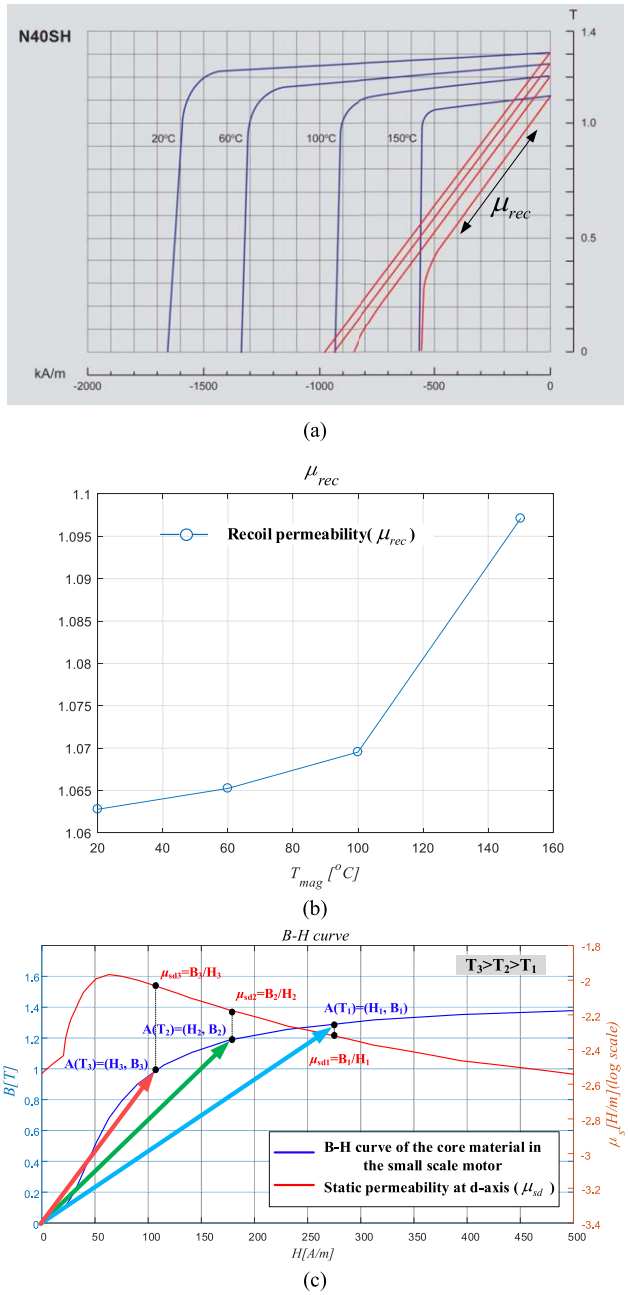

Fig. 2. Recoil permeability of the magnet (N40SH) and permeability of the core used in the small-scale motor. (a) B–H curve of the magnet. (b) Recoil permeability of the magnet ($\mu_{\rm rec}$). (c) B–H curve of core material and permeability.

obtained from the slope of the normal curve. The calculated permeability with respect to the magnet temperature is shown in Fig. 2(b). From this figure, a derivative of $\mu_{\rm rec}$ with respect to $T_{\rm mag}$, $\alpha_{\mu \rm rec}$, in (6) is positive [1]. A static relative permeability of silicon steel in the core, μ_{rc}, is also strongly affected by the magnet temperature because an operation point influences the permeability on a B–H curve of core material in the small-scale motor, denoted as arrows in Fig. 2(c). The figure shows an operation point shift in the sequence of A($\rm T_1$), A($\rm T_2$), and A($\rm T_3$) when the temperature increases from $\rm T_1$ to $\rm T_2$ and from $\rm T_2$ to $\rm T_3$. As a result, permeability, μ_{sd}, denoted as a red line in the figure, increases from $\mu_{\rm sd1}$ to $\mu_{\rm sd3}$ due to the operation point shift by the magnet temperature increasing, as shown in Fig. 2(c). Therefore, in (6), the derivative of μ_{rc} with respect to $T_{\rm mag}$, $\alpha_{\mu rc}$, is also positive. Through the analysis, it is found that a derivative of reluctance by the magnet temperature, $dR/dT_{\rm mag}$, is always negative. In other words, the inductances increase when the magnet temperature increases because the variation of inductance caused by the magnet temperature is directly proportional to the inverse of the reluctance (6).

In order to demonstrate the relationship between inductances and the magnet temperature, an experiment has been designed and executed in the motor. The IPMSM model in the rotor reference frame is given in (2). In steady state, the differential terms in (2) can be eliminated, and the flux linkages can be obtained from (7) [37]. In the experiment, the q-axis current has been regulated by null for removing the resistance effect and getting accurate d-axis flux by (8), where d-axis voltage reference, v_{ds}^{r*}, and q-axis voltage reference, v_{qs}^{r*}, are used instead of v_{ds}^{r} and v_{qs}^{r} in (7). In (8), low pass filter (LPF) is the abbreviation of a low pass filter. The cutoff frequency of the LPF is low enough to suppress harmonics, including the spatial harmonics and obtain dc components of d-axis and q-axis flux linkages, λ_{ds0}^{r} and λ_{qs0}^{r}. During the settling time, the magnet temperature and stator temperature would vary. Therefore, the cutoff frequency should be set as an appropriate value. In this article, first-order low pass filter is employed, and its cutoff frequency is 11.3 rad/s.

$$\begin{aligned}\lambda_{qs}^{r} &= \frac{-v_{ds}^{r} + R_s i_{ds}^{r}}{\omega_r} \\ \lambda_{ds}^{r} &= \frac{v_{qs}^{r} - R_s i_{qs}^{r}}{\omega_r} \qquad (7) \\ \lambda_{ds0}^{r} &= \mathrm{LPF}\left(\frac{v_{qs}^{r*} - R_s i_{qs}^{r}}{\omega_r}\right) \\ \lambda_{qs0}^{r} &= \mathrm{LPF}\left(\frac{-v_{ds}^{r*} + R_s i_{ds}^{r}}{\omega_r}\right). \qquad (8)\end{aligned}$$

The experiment results at a rotating speed of 700 r/min are shown in Fig. 3(a). In this figure, when the d-axis current is null, the d-axis flux has only the magnet flux linkage by (2). In this condition, the $\alpha_{\rm mag}$ in (1) is obtained as $-0.096\%/^{\circ}\rm C$ in the experiment. Also, the d-axis inductance can be calculated from Fig. 3(a), which is shown in Fig. 3(b). A red arrow in Fig. 3(b) represents the direction of temperature increase. The d-axis inductance variation with respect to the temperature can be described as (9), where α_{Lds} is an average sensitivity of inductance with respect to the magnet temperature. The α_{Lds} is shown in Fig. 3(c), and it is larger than that of $\alpha_{\rm mag}$ in Fig. 3(a). It means that the inductance variation could be a considerable component in the magnet temperature estimation.

$$L_{ds}\left(T_{\rm mag}\right) = L_{ds}\left(20^{o}\rm C\right)\left(1 + \alpha_{Lds}\left(T_{\rm mag} - 20^{o}\rm C\right)\right). \qquad (9)$$

This static inductance variation in (9) comes from changing the saturation level of the core by the magnet temperature. These saturation level variations have been exploited in the low-speed region because the magnet flux linkage cannot be used in low

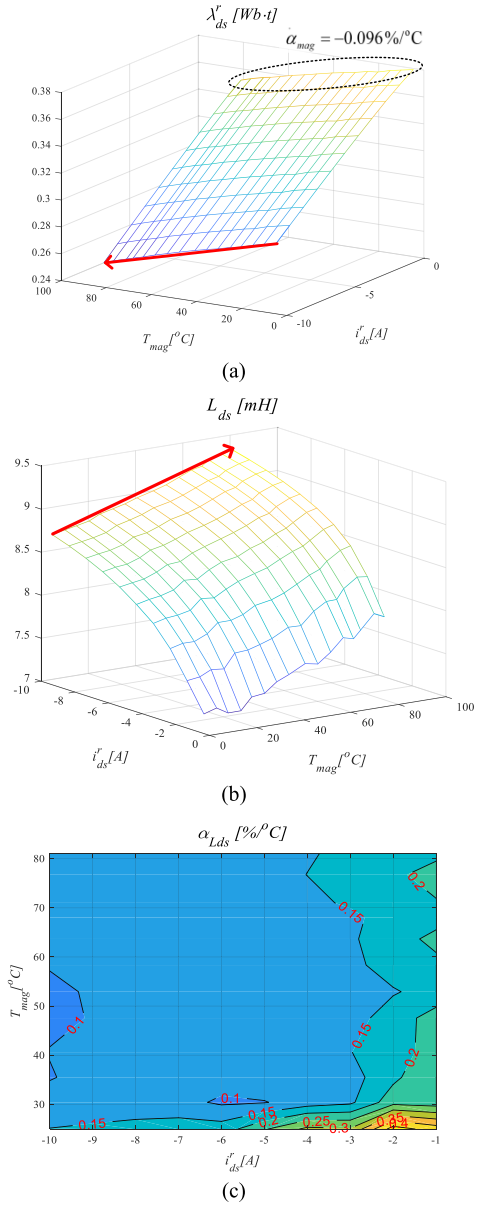

Fig. 3. Inductance variation with the magnet temperature in experimental results. (a) *D*-axis flux. (b) *D*-axis inductance. (c) Average sensitivity of inductance with respect to the magnet temperature, α_{Lds}.

speed, [15]–[17] and [21], [22]. Especially, high-frequency inductance was directly used in [21], [22]. In this article, the static inductances variations like (9) have been used in addition to the magnet flux linkage variation caused by the magnet temperature as a form of reactive energy.

B. Fundamental Reactive Energy and the Magnet Temperature

In this article, fundamental reactive energy, $E_{\text{react}\,0}$, has been directly utilized. The fundamental reactive energy is defined as fundamental reactive power, Q_0, divided by rotating speed, ω_{r0}, in (10). In this equation, λ^r_{ds0} and λ^r_{qs0} are fundamental components of *d*-axis flux and *q*-axis flux. By substituting the fluxes by using inductive components and the magnet flux linkage as (2), the reactive energy can be presented in terms of the inductances and magnet flux linkage.

$$\begin{aligned} E_{\text{react0}}[\text{VAR}\cdot s] = \frac{Q_0}{1.5\omega_{r0}} &= \lambda^r_{ds0}\left(i^r_{ds0},\, i^r_{qs0}\right) i^r_{ds0} \\ &+ \lambda^r_{qs0}\left(i^r_{ds0},\, i^r_{qs0}\right) i^r_{qs0} \\ &= L_{ds}\left(i^r_{ds0},\, i^r_{qs0}\right) i^{r2}_{ds0} + \lambda_{pm0} i^r_{ds0} \\ &+ L_{qs}\left(i^r_{ds0},\, i^r_{qs0}\right) i^{r2}_{qs0}. \end{aligned} \tag{10}$$

The fundamental reactive energy is also varied with the magnet temperature. The derivative of the fundamental reactive energy with respect to the magnet temperature can be represented as (11). In this equation, first and second terms in the right-hand side, inductance variation terms, are positive because the inductances are inverse of reluctance, and the derivative of reluctance with respect to the magnet temperature is negative in (6), as explained in the Section III-A. The third term is larger than null because α_{mag} is negative, and the fundamental *d*-axis current i^r_{ds0} is less than null in normal operation points of an IPMSM for traction.

$$\begin{aligned} &\frac{\partial E_{\text{react0}}\left(i^r_{ds0},\, i^r_{qs0},\, T_{\text{mag}}\right)}{\partial T_{\text{mag}}} \\ &= \frac{\partial L_{ds}\left(i^r_{ds0},\, i^r_{qs0},\, T_{\text{mag}}\right)}{\partial T_{\text{mag}}} i^{r2}_{ds0} \\ &+ \frac{\partial L_{qs}\left(i^r_{ds0},\, i^r_{qs0},\, T_{\text{mag}}\right)}{\partial T_{\text{mag}}} i^{r2}_{qs0} + \alpha_{\text{mag}} \lambda_{pm0} i^r_{ds0}. \end{aligned} \tag{11}$$

The fundamental reactive energy has an inherent limitation. The reactive energy is null under a no-load condition, as seen from (10). Therefore, in a no-load condition, this method cannot estimate the magnet temperature.

C. Fundamental Reactive Energy and Stator Winding Resistance

When calculating fluxes by using (8), stator winding resistance, R_s, is utilized. R_s varies according to a stator winding temperature, T_{sw}, in (12), where R_{s_20} is the value of R_s at 20 °C. If $\Delta R_s(T_{sw})$, which is the stator winding resistance variation caused by T_{sw}, is not compensated, then the fluxes are calculated with errors, which is denoted as $\lambda^r_{ds\_\text{hat}}$ and $\lambda^r_{qs\_\text{hat}}$ in (13). The errors can be calculated in (14). These terms could make no negligible estimation errors. Therefore, the stator winding temperature has been measured in [23]–[26] to compensate for the flux errors caused by the stator resistance variation. In these methods, the stator winding temperature sensors should be installed in a motor.

$$\begin{aligned} &R_s = R_{s\_20}\left(1 + \alpha_{cu}\left(T_{sw} - 20^oC\right)\right) = R_{s\_20} + \Delta R_s\left(T_{sw}\right), \\ &\text{where } \Delta R_s\left(T_{sw}\right) = \alpha_{cu} R_{s\_20}\left(T_{sw} - 20^oC\right) \end{aligned} \tag{12}$$

$$\begin{aligned} \lambda^r_{ds\_hat} &= \left(\frac{v^r_{qs} - R_{s\_20} i^r_{qs}}{\omega_r}\right) \quad \text{and} \\ \lambda^r_{qs\_\text{hat}} &= \left(-\frac{v^r_{ds} - R_{s\_20} i^r_{ds}}{\omega_r}\right) \end{aligned} \tag{13}$$

where R_{s_20} is a stator winding resistance at 20 °C.

$$\lambda_{ds}^{r} - \lambda_{ds\_\mathrm{hat}}^{r} = -\left(\frac{\Delta R_s\left(T_{sw}\right) i_{qs}^{r}}{\omega_r}\right)$$
$$\lambda_{qs}^{r} - \lambda_{qs\_\mathrm{hat}}^{r} = \left(\frac{\Delta R_s\left(T_{sw}\right) i_{ds}^{r}}{\omega_r}\right). \tag{14}$$

The stator resistance might vary by a rotating speed, which is called as the ac resistance effect [32]. It is reported that the ac resistance effect has a considerable influence on stator resistance in a motor with hairpin type stator winding, which is widely employed in a traction motor [32]. However, the conventional method in [23]–[26] compensates only the stator resistance variation due to not the rotating speed but the stator temperature variation by measuring the stator winding temperature. It might cause considerable errors in the estimation of the temperature in a traction motor with hairpin type winding. In this article, it can be expected that the stator resistance variation caused by the ac resistance effect can make the flux errors in the same process in (14).

However, in the proposed method, the fluxes are not directly used. The reactive energy can be calculated with the stator resistance error, R_{s_err}, including $\Delta R_s(T_{sw})$ in (12) and the ac resistance effect are inherently removed in (15), which is the same principle in [33]. It means that no temperature sensor at stator winding is required to estimate the magnet temperature in the proposed method.

$$\begin{aligned} E_{\mathrm{react0}}[\mathrm{VAR}\cdot s] &= \frac{Q_0}{1.5\omega_r} \\ &= \frac{R_{s\_err} i_{qs0}^{r} + \omega_r \lambda_{ds0}^{r}\left(i_{ds0}^{r},\, i_{qs0}^{r}\right)}{\omega_r} i_{ds0}^{r} \\ &\quad - \frac{R_{s\_err} i_{ds0}^{r} - \omega_r \lambda_{qs0}^{r}\left(i_{ds0}^{r},\, i_{qs0}^{r}\right)}{\omega_r} i_{qs0}^{r} \\ &= \lambda_{ds0}^{r}\left(i_{ds0}^{r},\, i_{qs0}^{r}\right) i_{ds0}^{r} + \lambda_{qs0}^{r}\left(i_{ds0}^{r},\, i_{qs0}^{r}\right) i_{qs0}^{r}. \end{aligned} \tag{15}$$

D. Fundamental Reactive Energy and Inverter's Nonlinearity Effect

The d-axis voltage, v_{ds}^{r*}, and q-axis voltage, v_{qs}^{r*}, are used in calculating the fluxes in (8) under the assumption that an inverter accurately synthesizes voltages, and these fluxes are used to calculate the reactive energy by (10). However, due to the inverter nonlinearity effect, output voltages of an inverter, v_{ds}^{r} and v_{qs}^{r}, are not the same as reference voltages, v_{ds}^{r*} and v_{qs}^{r*}. The voltage error due to the inverter nonlinearity effect at x-phase, $\delta \mathrm{v}_{xn}$, can be defined in (16), where x is a certain phase among a-, b-, and c-phases. The x-phase voltage error can be approximated as an arctangent function with $\mathrm{V_{sat}}$ and $\mathrm{K_{atan}}$, which are tuning factors, [36]. A scaling factor, k_{xt}, is newly defined in (16), which is usually unity. Fig. 4 shows the nonlinearity effect of the inverter used in experiments. In this figure, the approximation accurately represents the inverter's nonlinearity effect

$$\delta \mathrm{v}_{xn} = v_{xn}^{*} - \mathrm{v}_{xn} = \frac{2\mathrm{V_{sat}} k_{xt}}{\pi} \cdot \mathrm{atan}(\mathrm{K_{atan}} \cdot i_{xs}). \tag{16}$$

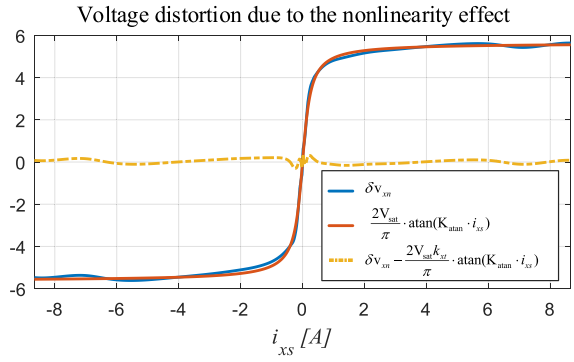

Fig. 4. Nonlinearity effect measured in the inverter connected to the small-scale motor.

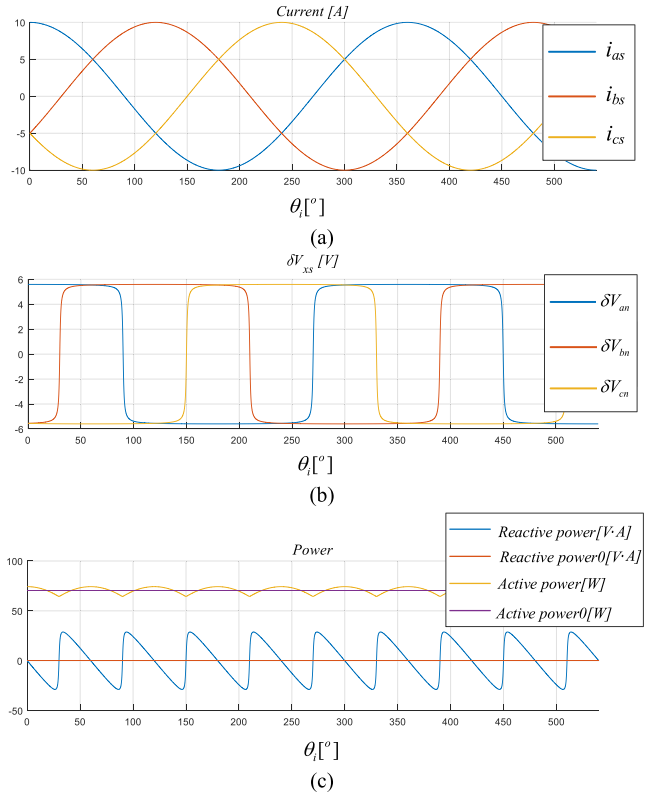

Fig. 5. Inverter nonlinearity effect on the proposed method analyzed by simulations when $k_{at} = 1$, $k_{bt} = 1$, and $k_{ct} = 1$ in (16), where x-axis is an angle of current, θ_i. (a) Three phase currents, i_{as}, i_{as}, and i_{cs}. (b) Three phase voltage distortions due to the inverter nonlinearity effect in (16), $\delta \mathrm{v_{an}}$, $\delta \mathrm{v_{bn}}$, and $\delta \mathrm{v_{cn}}$. (c) Reactive power, active power, and their average values.

By using this approximated model in Fig. 4, the fundamental reactive energy error caused by the nonlinearity effect can be simulated. Fig. 5 is a simulation result when the inverter nonlinearity effect with $k_{at} = k_{bt} = k_{ct} = 1$. It means that $\delta \mathrm{v}_{an}$, $\delta \mathrm{v_{bn,}}$ and $\delta \mathrm{v}_{cn}$ are balanced voltages, as shown in Fig. 5(b). In cases of $k_{at} = 1.2$, $k_{bt} = 1$, $k_{ct} = 0.8$, $\delta \mathrm{v}_{an}$, $\delta \mathrm{v}_{bn}$, and $\delta \mathrm{v}_{cn}$ are unbalanced as shown in Fig. 6(b). The fundamental reactive energy is denoted as "*Reactive power0,*" whose value is null in both cases in Figs. 5(c) and 6(c). It means that the calculated fundamental reactive energy is theoretically not affected by the

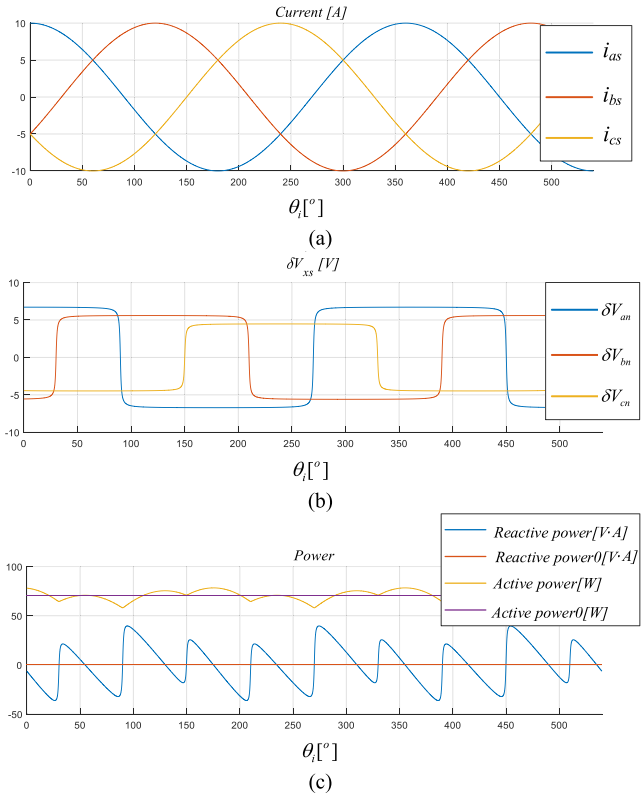

Fig. 6. Inverter nonlinearity effect on the proposed method analyzed by simulations when $k_{at} = 0.8$, $k_{bt} = 1$, and $k_{ct} = 1.2$ in (16), where x-axis is an angle of current, θ_i. (a) Three phase currents, i_{as}, i_{as}, and i_{cs}. (b) Three phase voltage distortions due to the inverter nonlinearity effect in (16), $\delta \mathrm{v_{an}}$, $\delta \mathrm{v_{bn}}$, and $\delta \mathrm{v_{cn}}$. (c) Reactive power, active power, and their average values.

inverter nonlinearity effect. These results explain that the fundamental components of voltage distortion due to the nonlinearity effect are in phase with the current. Therefore, it can be modeled as a stator resistance component. It results in changing not the fundamental reactive energy but the fundamental active energy. However, in the experiment, the nonlinearity effect generates harmonics, which make the phase delay in the voltage distortion, δv_{xn}. This delay makes the nonlinearity effect influence the fundamental reactive energy, which results in the estimation error. This effect is too complex to analyze in the simulation and small enough to be negligible. The effect is shown in the experimental result in Section V instead of the simulation result.

E. Implementation of a Magnet Temperature Estimator

In this section, a temperature estimator is implemented based on the fundamental reactive energy. The fluxes can be modeled as functions of torque, speed, and the magnet temperature, where torque is a function of d-axis and q-axis currents. In this article, it is assumed that the currents are determined under maximum torque per ampere (MTPA) condition, and that the MTPA condition is not changed according to the magnet temperature and speed to simplify the implementation and verification of the proposed method. The fluxes can be approximated by a second-order polynomial of the magnet temperature with coefficients in (17). The coefficients will be found and shown in the next section.

$$\begin{aligned}\lambda_{ds}^{r} &= A_d\left(T_e,\, \omega_{\mathrm{rpm}}\right) T_{\mathrm{mag}}^2 + B_d\left(T_e,\, \omega_{\mathrm{rpm}}\right) T_{\mathrm{mag}} \\ &\quad + C_d\left(T_e,\, \omega_{\mathrm{rpm}}\right) \\ \lambda_{qs}^{r} &= A_q\left(T_e,\, \omega_{\mathrm{rpm}}\right) T_{\mathrm{mag}}^2 + B_q\left(T_e,\, \omega_{\mathrm{rpm}}\right) T_{\mathrm{mag}} \\ &\quad + C_q\left(T_e,\, \omega_{\mathrm{rpm}}\right). \end{aligned} \tag{17}$$

Fig. 7 shows a block diagram of the proposed temperature estimator. Voltage references, v_{ds}^{r*} and v_{qs}^{r*}, are used instead of actual voltages. Instead of the actual current, the current reference is utilized for the calculation of the reactive energy because the current reference might be dc component of actual current in steady state and actual current would have a lot of ripple components, which are not the fundamental frequency components. Otherwise, a low pass filter should be employed to extract the dc value of the currents. By using these components and coefficients, the calculated fundamental reactive energy, $E_{\mathrm{react\_cal}}$ and the estimated fundamental reactive energy $E_{\mathrm{react\_est}}$ can be calculated from (18) and (19), respectively.

$$\begin{aligned} E_{\mathrm{react\_cal}} &= \frac{v_{qs}^{r} i_{ds0}^{r} - v_{ds}^{r} i_{qs0}^{r}}{\omega_{r0}} \\ &= \frac{v_{qs}^{r*} i_{ds}^{r*} - v_{ds}^{r*} i_{qs}^{r*}}{\omega_{r0}} = \frac{v_{qs}^{r*} i_{ds}^{r*} - v_{ds}^{r*} i_{qs}^{r*}}{k_{\mathrm{rpm2r}} \times \omega_{\mathrm{rpm0}}} \\ \text{where } k_{\mathrm{rpm2r}} &= \frac{2\pi}{60} \times \text{pole pair}. \end{aligned} \tag{18}$$

$$\begin{aligned} E_{\mathrm{react\_est}} &= A_{er} {T_{\mathrm{mag\_est}}}^2 + B_{er} T_{\mathrm{mag\_est}} + C_{er}, \\ \text{where } A_{er} &= A_d i_{ds}^{r} + A_q i_{qs}^{r}, \quad B_{er} = B_d i_{ds}^{r} + B_q i_{qs}^{r} \\ &\text{and } \; C_{er} = C_d i_{ds}^{r} + C_q i_{qs}^{r}. \end{aligned} \tag{19}$$

The estimated magnet temperature, $T_{\mathrm{mag\_est}}$, is obtained from a closed-loop function of the estimator, which is configured by using an integrator. The closed-loop function can be represented as (20), which is first-order low pass filter. The integral gain, k_{iE}, can be determined by (21). The bandwidth is set as 1 rad/s. It means that the estimator can reach 95% of the final estimated magnet temperature after three seconds, which would be the real temperature if there is no steady-state error.

$$\frac{T_{\mathrm{mag\_est}}}{T_{\mathrm{mag}}} = \frac{\left(2A_{er} T_{\mathrm{mag\_est}} + B_{er}\right) k_{iE}}{s + \left(2A_{er} T_{\mathrm{mag\_est}} + B_{er}\right) k_{iE}} = \frac{\omega_T}{s + \omega_T} \tag{20}$$

$$k_{iE} = \frac{\omega_T}{2A_{er} T_{\mathrm{mag\_est}} + B_{er}}. \tag{21}$$

V. Experiment Results

Fig. 8(a) and (b) shows the fundamental components of calculated d-axis flux linkage, $\lambda_{ds\_hat0}^{r}$, and q-axis flux linkage, $\lambda_{qs\_hat0}^{r}$, in the small-scale motor, which are dc components extracted from (13) by using the same low pass filter in (8). Rotating speed varies from 700 to 1700 r/min, and torque varies from no load to full load (10 N·m) following the MTPA line. In $\lambda_{ds\_hat0}^{r}$ and $\lambda_{qs\_hat0}^{r}$, the stator resistance error due to variation of stator temperature in (14) is included. The error due to

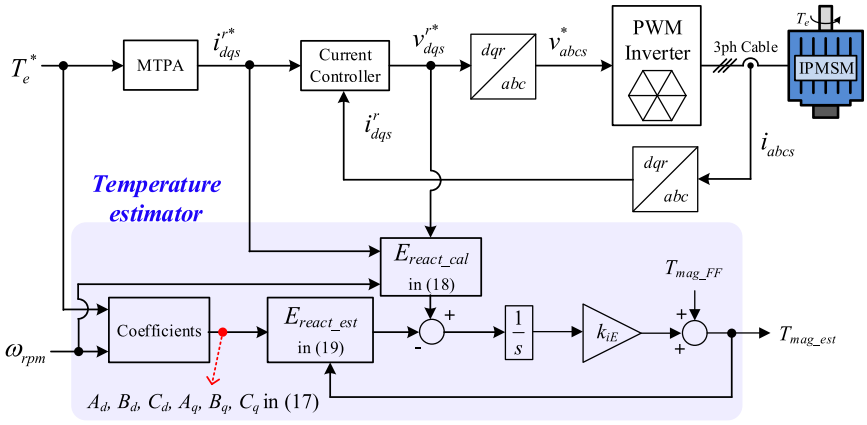

Fig. 7. Block diagram of the overall system with the proposed temperature estimator.

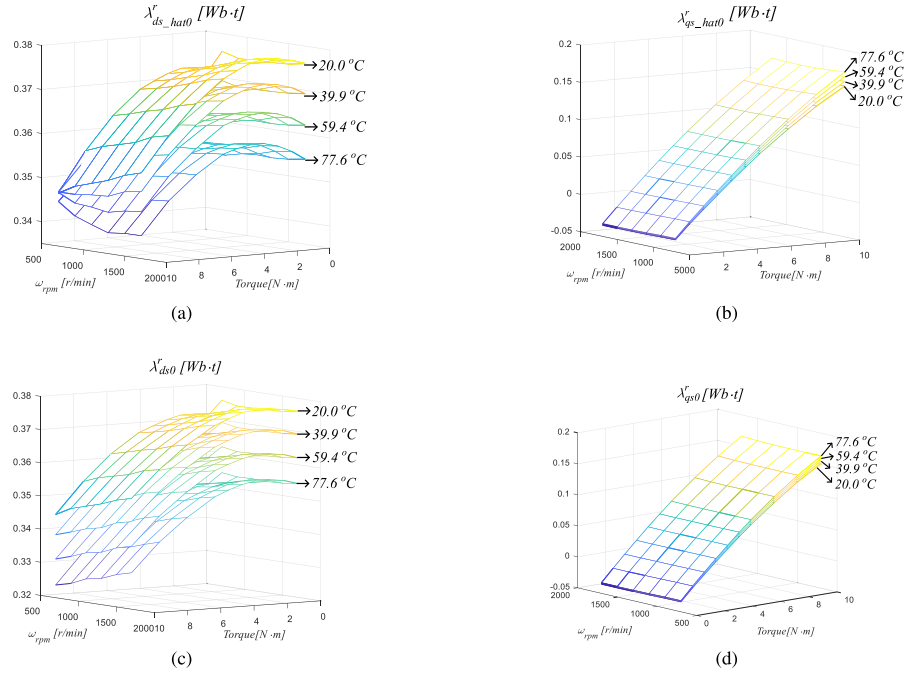

Fig. 8. Calculated fluxes. (a) $\lambda^r_{ds\_hat0}$. (b) $\lambda^r_{qs\_hat0}$. (c) λ^r_{ds0}. (d) λ^r_{qs0}.

stator resistance can be eliminated by using measured stator temperature, and λ^r_{ds0} and λ^r_{qs0} are achieved like (8). These results are shown in Fig. 8(c) and (d). Through a comparison of Fig. 8(a) and (c), it can be said that calculated fluxes are severely contaminated with the stator resistance error. Therefore, to apply conventional methods in [23]–[26], the stator resistance error should be considered and decoupled. The reactive energy is exactly the same regardless of whether fluxes include the resistance error or not by (15). In other words, the reactive energy is not affected by the stator resistance variations. As a result, the magnet temperature can be estimated by using the reactive energy without information of stator winding temperature.

Fig. 9(a) and (b) shows the measured flux linkages and the curves fitted by a second-order polynomial with respect to the magnet temperature at rated torque, 10 N·m and 1700 r/min. In this figure, red dots are measured data, and the blue line is a trend curve fitted as a second-order polynomial. By this process, the coefficients in (17) are achieved, as shown in Fig. 10. These coefficients are implemented as look-up tables (LUTs), in the coefficients block in Fig. 7. Installation of the LUTs would be a burden to a DSP. The maximum estimation error can be calculated with these coefficients by using (22), and the result is shown in Fig. 11(a). The maximum error is about 2.6 °C.

$$T_{\mathrm{mag\_err\_max}} = \mathrm{MAX}\left(\left|T_{\mathrm{mag}} - \frac{-B_{er} + \sqrt{{B_{er}}^2 - 4A_{er}C_{er}}}{2A_{er}}\right|\right). \quad (22)$$

The conventional method in [27] does not consider the inductance variation in Section III, which would result in a colossal error. The estimation error with the conventional method can be calculated as (23). The results are shown in Fig. 11(b). The

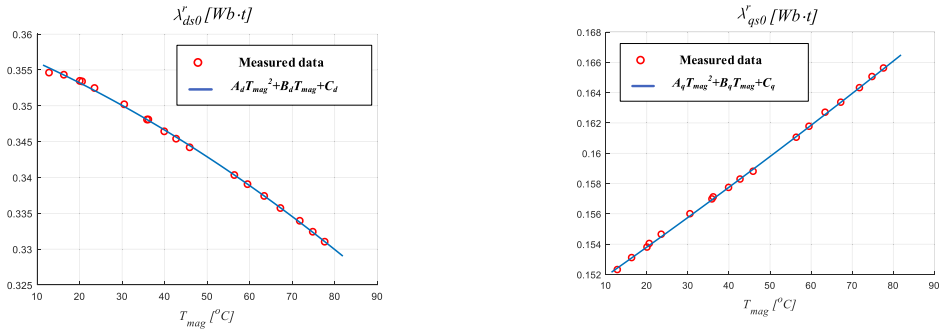

Fig. 9. Curve fitted flux linkages by second-order polynomials with respect to the magnet temperature. (a) D-axis flux linkage. (b) Q-axis flux linkage.

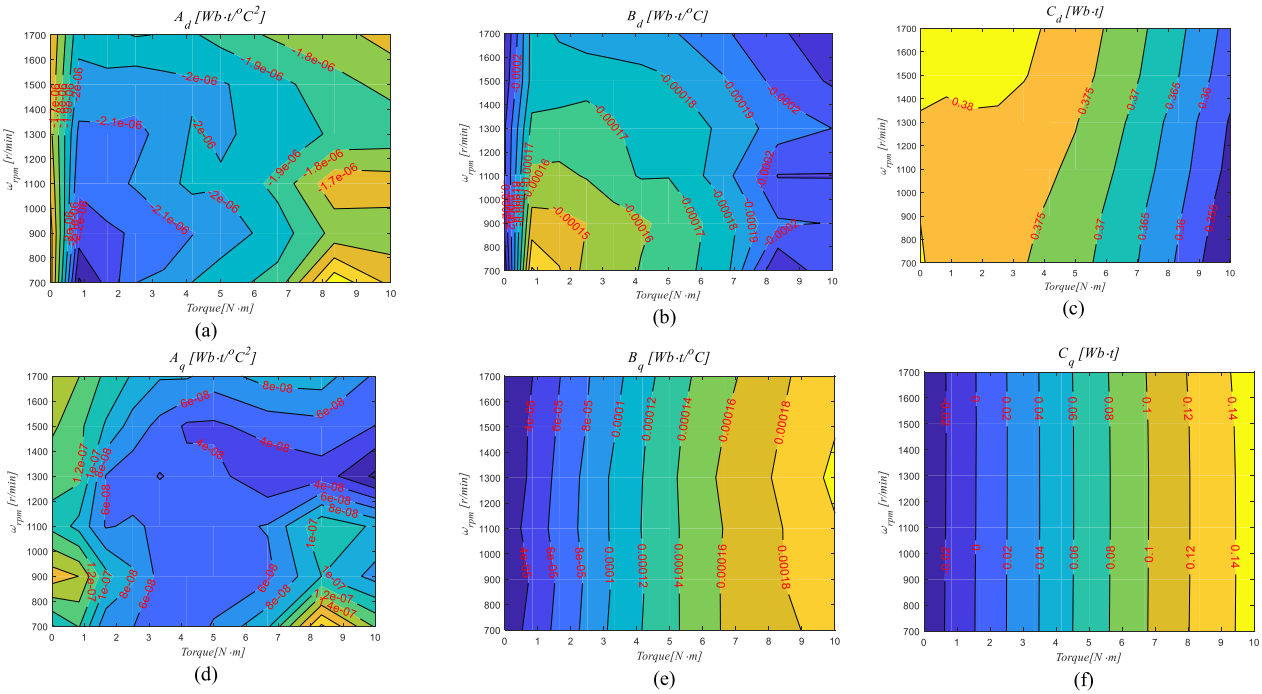

Fig. 10. Coefficients in (17) extracted from experimental test. (a) A_d. (b) B_d. (c) C_d. (d) A_q. (e) B_q. (f) C_q.

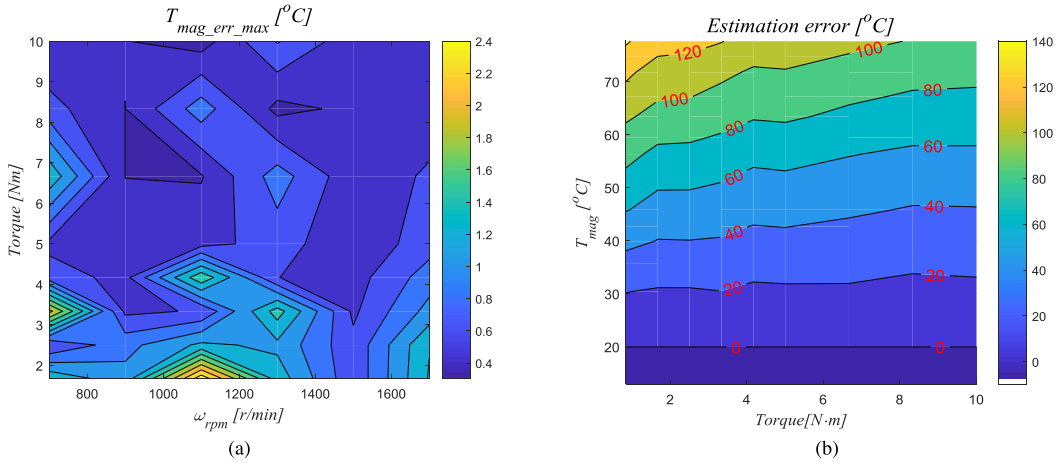

Fig. 11. Estimation errors of the proposed method and the conventional method. (a) Maximum estimation error with the proposed method by (22). (b) Estimation error conventional method by (23) at 1100 r/min.

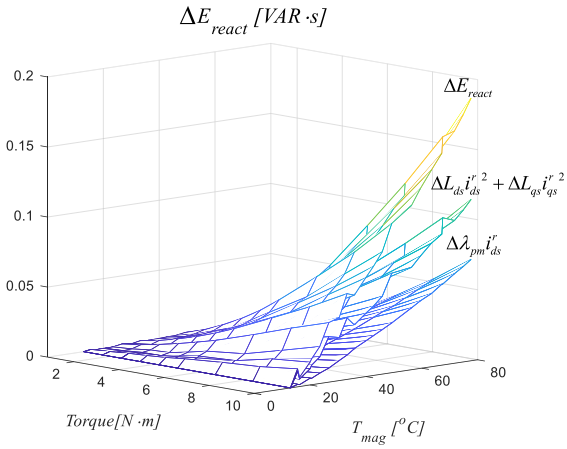

Fig. 12. Components in the fundamental reactive energy variation.

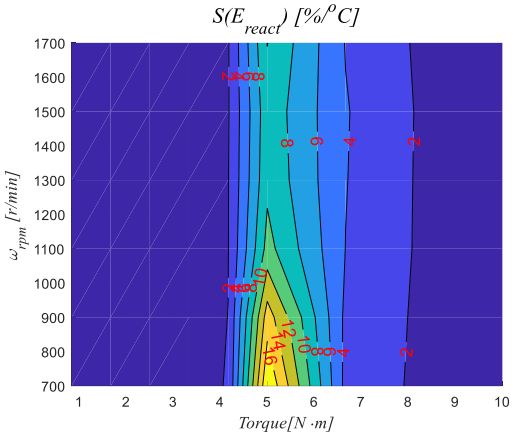

Fig. 13. Sensitivity of the proposed method.

estimation error with the conventional method increases over 140 °C. It can be explained by Fig. 12. In the reactive energy variation, there are two components, a magnet flux linkage variation term, $\Delta\lambda_{pm}i_{ds}^r$, and the inductance variation term, $\Delta L_{ds}{i_{ds}^r}^2 + \Delta L_{qs}{i_{qs}^r}^2$. The conventional method only used the magnet flux linkage variation component, and the inductance variation component was neglected.

$$T_{\text{mag\_err}} = T_{\text{mag\_est}} - T_{\text{mag}} = \frac{Q_0\left(T_{\text{mag}}\right) - Q_0\left(20^oC\right)}{\omega_{r0} i_{ds0}^r \lambda_{pm\_20} \alpha_{\text{mag}}} + 20^o\text{C} - T_{\text{mag}}. \quad (23)$$

Moreover, the inductive component increases with the magnet temperature increase, like the magnet flux component, which coincides with the analysis in (9). It results in that the fundamental reactive energy is sensitive enough to be used in the estimation. It can be demonstrated by calculating the sensitivity of the reactive energy, S(E_{react}). The sensitivity is calculated by (24) and shown in Fig. 13. The calculated sensitivity is larger than 0.2%/°C, which is the minimum value in Fig. 13. The conventional method uses only the magnetic flux linkage, and its sensitivity is determined as α_{mag}, whose value in

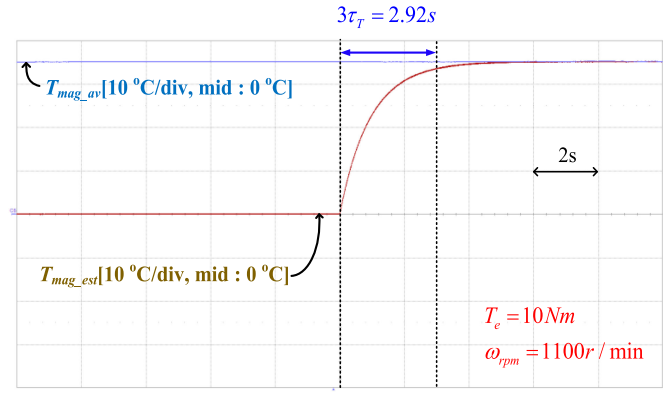

Fig. 14. Bandwidth test of the temperature estimator at 10 N·m and 1100 r/min.

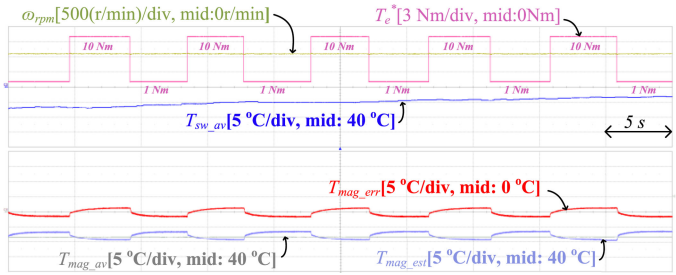

Fig. 15. Transient performance of the temperature estimation at repetitive step torques command.

the motor used in this experiment is −0.096%/°C, as shown in Fig. 3(a).

$$\text{Sensitivity of } x = S(x) = \frac{x\left(T_{\text{mag}}\right) - x\left(20^oC\right)}{T_{\text{mag}} - 20^oC} \frac{100}{x\left(20^oC\right)} \left[\%/^\circ\text{C}\right]. \quad (24)$$

The magnet temperature has been estimated in real time by using the proposed method to verify the effectiveness and validity of the proposed method. First, an experiment has been done to confirm the bandwidth of the estimator. The bandwidth of the proposed temperature estimator is shown in Fig. 14, when torque and speed are 10 N·m and 1100 r/min, respectively. In this figure, after 2.92 s, the estimated magnet temperature has reached 95% of the final value, which is the measured magnet temperature. As a result, the estimator can estimate the magnet temperature as designed bandwidth by using (21).

A step torque is repeatedly applied 1 to 10 N·m, to demonstrate transient performance. In Fig. 15, the estimation error varies according to repetitive step torques. However, the maximum error is less than 2 °C.

Fig. 16 shows the inverter nonlinearity effect on the online estimation by using the proposed method at 1100 r/min and the rated torque, 10 N·m. On the left side of a black dashed line in Fig. 16, the nonlinearity is compensated by using the arctangent function, as shown in Fig. 4. On the right side of the black dashed line, the inverter nonlinearity is not compensated.

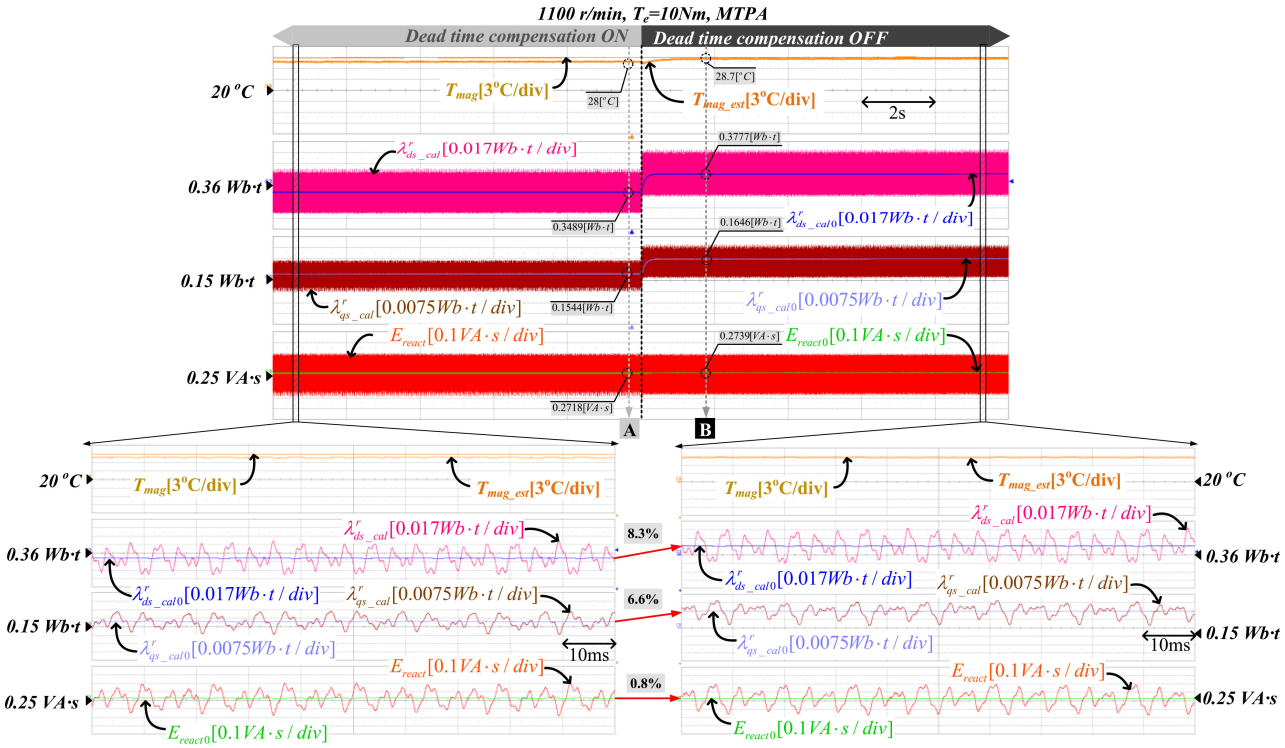

Fig. 16. Temperature estimation error due to the inverter nonlinearity effect at 1100 r/min and 10 N·m in the online estimation.

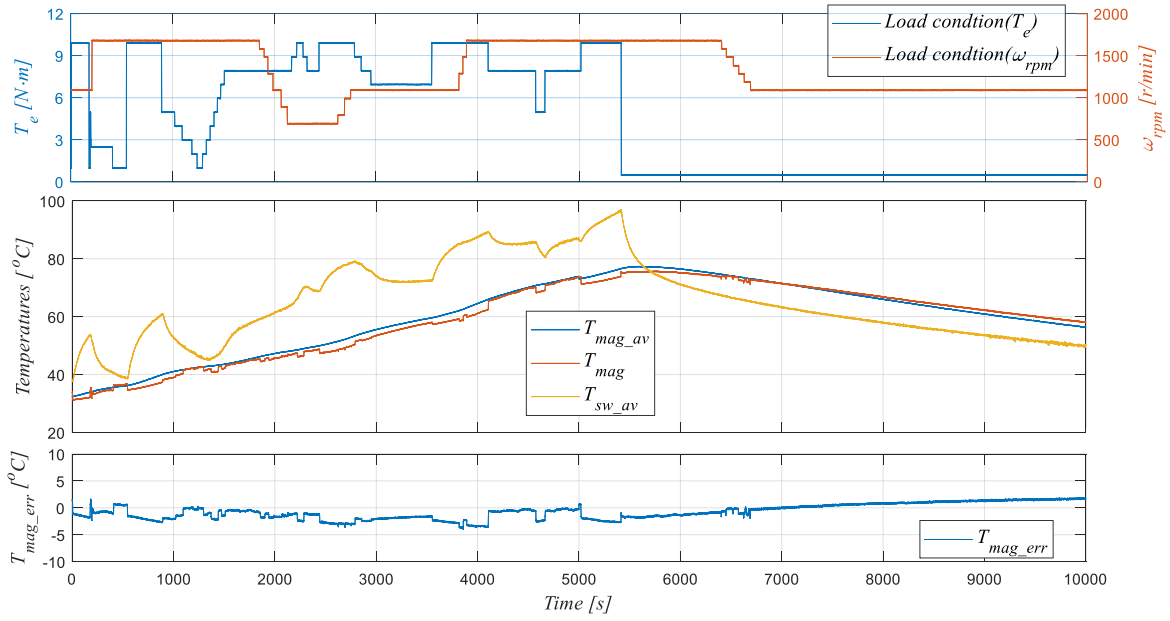

Fig. 17. Experimental results of the online estimation by using the proposed method for 10 000 s (=2.8 h).

A and B in Fig. 4 are the steady-state points of the left side, and right side of the black dashed line, respectively. Differences in d-axis and q-axis fluxes between A and B are 8.3% and 6.6%, respectively. This difference comes from only the inverter nonlinearity effect because the other conditions are the same, including the magnet temperature and the stator temperature. If the magnet flux linkage is calculated from the d-axis flux linkage in [23]–[26], the magnet temperature error, $T_{\mathrm{mag\_err}}$, can be obtained from (25), which is about 81 °C. Therefore, the change in d-axis flux linkage would make a considerable error in the estimation in previous studies.

$$T_{\mathrm{mag\_err}} = \frac{\lambda^r_{ds@A} - \lambda^r_{ds@B}}{\alpha_{\mathrm{mag}}\lambda_{pm\_20}}. \tag{25}$$

When the operating point is changed from A to B, the estimated magnet temperature slightly increases from 28 to 28.7 °C. In other words, the fundamental reactive energy slightly increases by 0.8% from A to B. It is because the nonlinearity effect can generate harmonics, which make the phase delay in the voltage distortion, δv_{xn}. This delay makes the nonlinearity effect influence the fundamental reactive energy and estimation error. In this experiment, the inverter nonlinearity effect increases the reactive energy due to this phase delay. As a result, the estimated temperature increases, which reduces an estimation error in this case.

The magnet temperature has been estimated in real time by using the proposed method to verify the effectiveness and validity of the proposed method. This online temperature estimation in Fig. 17 has been done for 10 000 s, where an abbreviation of "mid" represents the center values of each waveform. The measured stator winding temperature, denoted as a blue line in this figure, is plotted with a scale of 16 °C per division, which is twice the measured magnet temperature's division, denoted as an orange line. In this figure, there exists a discontinuous point in the waveforms at 5000 s to save the waveforms. The magnet temperature increases from 33 to 78 °C. After the stator winding temperature reaches 98 °C, cooling starts, and load torque and speed are kept as low, which results in decreasing both temperatures to about 50 °C as fast as possible. In this condition, the error of estimation, $T_{\mathrm{mag\_err}}$, is less than 3.7 °C. The online estimation results in Fig. 17 demonstrate that the proposed method can estimate the magnet temperature even in torque variation, speed variation, and severe stator winding temperature variation.

VII. Conclusion

In this article, the fundamental reactive energy is defined and used to estimate the magnet temperature of IPMSM. Moreover, based on the concept, the magnet temperature estimation method has been proposed. In order to prove the relationship between the magnet temperature and the fundamental reactive energy, the experimental setup has been configured to measure the magnet temperature directly and accurately. Through the theoretical analysis and experimental verification, the correlation between the magnet temperature and the fundamental reactive energy has been demonstrated, and it is also clarified that the proposed method is robust to the practical issues such as the stator resistance variation due to the stator temperature, ac resistance effect, and inverter nonlinearity effect. Moreover, the proposed method has higher sensitivity because the variations of magnet flux linkage and inductances are simultaneously considered. As a result, regardless of wide speed and torque variations, the maximum estimation error is less than 3.7 °C during the online estimation for about 10 000 s without any temperature sensor at the stator winding.

References

[1] S. Constantinides, "Understanding and using reversible temperature coefficients," Arnold Magnetic Technologies, Rochester, NY, USA, 2009.

[2] M. Calin and E. Helerea, "Temperature influence on magnetic characteristics of NdFeB permanent magnets," in *Proc. 7th Int. Symp. Adv. Top. Elect. Eng. (ATEE), Bucharest*, 2011, pp. 1–6.

[3] S. Li, D. Han, and B. Sarlioglu, "Impact of temperature variation on fuel economy of electric vehicles and energy saving by using compensation control," in *Proc. IEEE Transp. Electrif. Conf. Expo.*, Long Beach, CA, USA, 2018, pp. 702–707.

[4] S. Li, B. Sarlioglu, S. Jurkovic, N. R. Patel, and P. Savagian, "Analysis of temperature effects on performance of interior permanent magnet machines for high variable temperature applications," *IEEE Trans. Ind. Appl.*, vol. 53, no. 5, pp. 4923–4933, Sep./Oct. 2017.

[5] S. Li, B. Sarlioglu, S. Jurkovic, N. R. Patel, and P. Savagian, "Comparative analysis of torque compensation control algorithms of interior permanent magnet machines for automotive applications considering the effects of temperature variation," *IEEE Trans. Transp. Electrif.*, vol. 3, no. 3, pp. 668–681, Sep. 2017.

[6] A. Rabiei, T. Thiringer, M. Alatalo, and E. A. Grunditz, "Improved maximum-torque-per-ampere algorithm accounting for core saturation, cross-coupling effect, and temperature for a pmsm intended for vehicular applications," *IEEE Trans. Transp. Electrif.*, vol. 2, no. 2, pp. 150–159, Jun. 2016.

[7] Y. Kim and S. Sul, "Torque control strategy of an ipmsm considering the flux variation of the permanent magnet," in *Proc. IEEE Ind. Appl. Annu. Meeting*, New Orleans, LA, USA, 2007, pp. 1301–1307.

[8] T. Sebastian, "Temperature effects on torque production and efficiency of PM motors using NdFeB magnets," *IEEE Trans. Ind. Appl.*, vol. 31, no. 2, pp. 353–357, Mar./Apr. 1995.

[9] G. D. Demetriades, H. Z. D. L. Parra, E. Andersson, and H. Olsson, "A real-time thermal model of a permanent-magnet synchronous motor," *IEEE Trans. Power Electron.*, vol. 25, no. 2, pp. 463–474, Feb. 2010.

[10] P. H. Mellor, D. Roberts, and D. R. Turner, "Lumped parameter thermal model for electrical machines of TEFC design," *IEE Proc. B - Electric Power Appl.*, vol. 138, no. 5, pp. 205–218, Sep. 1991.

[11] M. Kamiya, Y. Kawase, T. Kosaka, and N. Matsui, "Temperature distribution analysis of permanent magnet in interior permanent magnet synchronous motor considering PWM carrier harmonics," in *Proc. Int. Conf. Elect. Mach. Syst.*, Seoul, South Korea, 2007, pp. 2023–2027.

[12] N. Simpson, R. Wrobel, and P. H. Mellor, "An accurate mesh-based equivalent circuit approach to thermal modeling," *IEEE Trans. Magn.*, vol. 50, no. 2, pp. 269–272, Feb. 2014.

[13] T. Huber, W. Peters, and J. Böcker, "Monitoring critical temperatures in permanent magnet synchronous motors using low-order thermal models," in *Proc. Int. Power Electron. Conf.*, Hiroshima, Japan, 2014, pp. 1508–1515.

[14] C. Kral, A. Haumer, and S. B. Lee, "A practical thermal model for the estimation of permanent magnet and stator winding temperatures," *IEEE Trans. Power Electron.*, vol. 29, no. 1, pp. 455–464, Jan. 2014.

[15] M. Ganchev, C. Kral, and T. Wolbank, "Sensitivity and robustness aspects of sensorless rotor temperature estimation technique for permanent magnet synchronous motor," in *Proc. 15th Int. Power Electron. Motion Control Conf.*, Novi Sad, Serbia, 2012, pp. LS3a-1.2-1–LS3a-1.2-6.

[16] M. Ganchev, C. Kral, and T. Wolbank, "Sensorless rotor temperature estimation of permanent magnet synchronous motor under load conditions," in *Proc. 38th Annu. Conf. IEEE Ind. Electron. Soc.*, Montreal, QC, Canada, 2012, pp. 1999–2004.

[17] M. Ganchev, C. Kral, and T. M. Wolbank, "Compensation of speed dependence in sensorless rotor temperature estimation for permanent-magnet synchronous motor," *IEEE Trans. Ind. Appl.*, vol. 49, no. 6, pp. 2487–2495, Nov./Dec. 2013.

[18] D. D. Reigosa, F. Briz, P. Garcia, J. M. Guerrero, and M. W. Degner, "Magnet temperature estimation in surface PM machines using high-frequency signal injection," *IEEE Trans. Ind. Appl.*, vol. 46, no. 4, pp. 1468–1475, Jul./Aug. 2010.

[19] D. D. Reigosa, D. Fernandez, H. Yoshida, T. Kato, and F. Briz, "Permanent-magnet temperature estimation in pmsms using pulsating high-frequency current injection," *IEEE Trans. Ind. Appl.*, vol. 51, no. 4, pp. 3159–3168, Jul./Aug. 2015.

[20] D. Fernandez, M. Martínez, D. Diaz Reigosa, J. M. Guerrero, C. Manuel Suárez Alvarez, and F. Briz, "Influence of magnetoresistance and temperature on permanent magnet condition estimation methods using high-frequency signal injection," *IEEE Trans. Ind. Appl.*, vol. 54, no. 5, pp. 4218–4226, Sep./Oct. 2018.

[21] H. S. Jung, D. Park, H. Kim, S. Sul, and D. J. Berry, "Non-invasive magnet temperature estimation in IPMSM by high frequency pulsating sinusoidal voltage injection," in *Proc. IEEE Transp. Electrif. Conf. Expo.*, Long Beach, CA, USA, 2018, pp. 858–862.

[22] H. S. Jung, D. H. Park, H. G. Kim, S. K. Sul, and D. J. Berry, "Non-invasive magnet temperature estimation in IPMSM by using high frequency inductance with pulsating high frequency voltage signal injection," *IEEE Trans. Ind. Appl.*, vol. 55, no. 3, pp. 3076–3086, May/Jun. 2019.
[23] D. Reigosa, D. Fernandez, T. Tanimoto, T. Kato, and F. Briz, "Comparative analysis of BEMF and pulsating high-frequency current injection methods for pm temperature estimation in PMSMs," *IEEE Trans. Power Electron.*, vol. 32, no. 5, pp. 3691–3699, May 2017.
[24] A. Specht and J. Böcker, "Observer for the rotor temperature of IPMSM," in *Proc. 14th Int. Power Electron. Motion Control Conf.*, Ohrid, Macedonia, 2010, pp. T4–12–T4-15.
[25] A. Specht, O. Wallscheid, and J. Böcker, "Determination of rotor temperature for an interior permanent magnet synchronous machine using a precise flux observer," in *Proc. Int. Power Electron. Conf.*, Hiroshima, Japan, 2014, pp. 1501–1507.
[26] O. Wallscheid, A. Specht, and J. Böcker, "Observing the permanent-magnet temperature of synchronous motors based on electrical fundamental wave model quantities," *IEEE Trans. Ind. Electron.*, vol. 64, no. 5, pp. 3921–3929, May 2017.
[27] G. Feng, C. Lai, J. Tjong, and N. C. Kar, "Noninvasive Kalman filter based permanent magnet temperature estimation for permanent magnet synchronous machines," *IEEE Trans. Power Electron.*, vol. 33, no. 12, pp. 10673–10682, Dec. 2018.
[28] W. Kirchgässner, O. Wallscheid, and J. Böcker, "Empirical evaluation of exponentially weighted moving averages for simple linear thermal modeling of permanent magnet synchronous machines," in *Proc. IEEE 28th Int. Symp. Ind. Electron.*, Vancouver, BC, Canada, 2019, pp. 318–323.
[29] W. Kirchgässner, O. Wallscheid, and J. Böcker, "Deep residual convolutional and recurrent neural networks for temperature estimation in permanent magnet synchronous motors," in *Proc. IEEE Int. Electric Mach. Drives Conf.*, San Diego, CA, USA, 2019, pp. 1439–1446.
[30] O. Wallscheid, W. Kirchgässner, and J. Böcker, "Investigation of long short-term memory networks to temperature prediction for permanent magnet synchronous motors," in *Proc. Int. Joint Conf. Neural Netw.*, Anchorage, AK, USA, 2017, pp. 1940–1947.
[31] J. Lee and J. Ha, "Temperature estimation of PMSM using a difference-estimating feedforward neural network," *IEEE Access*, vol. 8, pp. 130855–130865, 2020.
[32] S. Jurkovic, K. M. Rahman, J. C. Morgante, and P. J. Savagian, "Induction machine design and analysis for general motors e-assist electrification technology," *IEEE Trans. Ind. Appl.*, vol. 51, no. 1, pp. 631–639, Jan./Feb. 2015.
[33] L. J. Garces, "Parameter adaption for the speed-controlled static ac drive with a squirrel-cage induction motor," *IEEE Trans. Ind. Appl.*, vol. IA-16, no. 2, pp. 173–178, Mar. 1980.
[34] H. S. Jung, H. G. Kim, S. K. Sul, and D. J. Berry, "Magnet temperature estimation of IPMSM by using reactive energy," in *Proc. 10th Int. Conf. Power Electron.*, Busan, South Korea, 2019, pp. 1–6.
[35] D. H. Park, H. S. Jung, H. J. Cho, and S. K. Sul, "Design of wireless temperature monitoring system for measurement of magnet temperature of IPMSM," in *Proc. IEEE Transp. Electrif. Conf. Expo.*, Long Beach, CA, 2018, pp. 656–661.
[36] D. W. Kim, Y. C. Kwon, S. K. Sul, J. H. Kim, and R. S. Yu, "Suppression of injection voltage disturbance for high-frequency square-wave injection sensorless drive with regulation of induced high-frequency current ripple," *IEEE Trans. Ind. Appl.*, vol. 52, no. 1, pp. 302–312, Jan./Feb. 2016.
[37] S. K. Sul, *Control of Electric Machine Drive Systems*. Hoboken, NJ, USA: Wiley, 2011.

Hyun-Sam Jung (Member, IEEE) received the B.S., M.S., and Ph.D. degrees in electrical engineering and computer science from Seoul National University, Seoul, South Korea, in 2010, 2012, and 2019, respectively.

From 2012 to 2015, he was with Samsung Heavy Industries Company Ltd., Suwon. From 2019 to 2020, he was with LG Electronics, Inc., Seoul. Since 2020, he has been an Assistant Professor with the Division of Electronics and Electrical Engineering, Dongguk University, Seoul. His current research interests include power electronics, control of electrical machines, and power converter circuits.

Hwigon Kim (Student Member, IEEE) received B.S degree in electrical engineering and computer science in 2018 from Seoul National University, Seoul, Korea, where he is currently working toward Ph.D. degree in electrical engineering.

His current research interests include control of power electronics and its application for electrical machines.

Seung-Ki Sul (Fellow, IEEE) received the B.S., M.S., and Ph.D. degrees in electrical engineering from Seoul National University, Seoul, South Korea, in 1980, 1983, and 1986, respectively.

From 1986 to 1988, he was an Associate Researcher with the Department of Electrical and Computer Engineering, University of Wisconsin, Madison, WI, USA. From 1988 to 1990, he was a Principal Research Engineer with LG Industrial Systems Company, South Korea. Since 1991, he has been a member of Faculty with the School of the Ele ctrical and Computer Engineering, Seoul National University, where he is currently a Professor. He has authored or coauthored more than 150 IEEE journal papers and a total of more than 340 international conference papers in the area of power electronics. His current research interests include position sensorless control of electrical machines, electric/hybrid vehicles and ship drives, and power converter circuits based on SiC MOSFET.

Dr. Sul was the Program Chair of IEEE Power Electronics Specialists Confer ence in 2006 and the General Chair of IEEE International Conference on Power Electronics and ECCE Asia in 2011. From 2011 to 2014, he was the Editor in Chief for the *Journal of Power Electronics*, which is an SCIE registered journal, published by the Korean Institute of Power Electronics (KIPE), Seoul, South Korea. In 2015, he was the President of KIPE. He was the recipient of the 2015 IEEE Transaction First and Second Paper Awards on Industrial Application, simultaneously. He was also the recipient of the 2016 Outstanding Achievement Award of the IEEE Industrial Application Society. He was also selected as the recipient of the 2017 Newell Award sponsored IEEE Power Electronics Society.

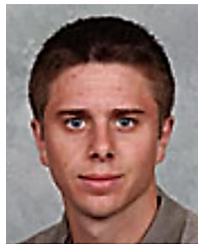

Daniel J. Berry received the B.S. degree in mechanical engineering and M.S. degree in controls engineering from Oakland University, Michigan, USA, in 2006 and 2010, respectively.

He is currently working with the General Motors in electric drive systems with background in mechanical design, heat transfer analysis, and electric machine controls. He holds several patents related to temperature estimation of electric drive traction motors.